The influence of separately and combined bentonite and kaolinite as binders for pelletization of NaA zeolite from coal fly ash

T. C. R. Bertolini[1], D. A. Fungaro[1]*, A. E. D. Mahmoud[2]
[1]Instituto de Pesquisas Energéticas e Nucleares, CNEN/SP, São Paulo, SP, Brazil
[2]Alexandria University, Faculty of Science, Environmental Sciences Department, Green Technology Group, 21511 Alexandria, Egypt

Abstract

Pelletization of zeolitic materials is required to facilitate their practical industrial and commercial applications. Zeolite-NaA was synthesized from fly ash by the fusion method and shaped into spherical granules. Bentonite, kaolinite, and a combination of bentonite with kaolinite were tested as binders with different contents from 5 to 10 wt%. The pellet formation was optimized. The physicochemical properties of binders, zeolite powder, and zeolite granular were characterized by X-ray fluorescence spectroscopy (XRF), X-ray diffraction (XRD), Fourier transform infrared spectroscopy (FTIR), nitrogen adsorption/desorption isotherm, and scanning electron microscopy (SEM) among other techniques. Deformation and breakage behavior of spherical granulates by compression was also studied. The best performance was obtained by the pellet with 10% bentonite with satisfactory mechanical strength and water resistance. The XRD and SEM results revealed NaA zeolite granular with a typical cubic shape and high crystallinity formed on the surface of bentonite. This result presents a potential use of the coal fly ash to obtain pelletized NaA zeolite following the principles of circular economy and the sustainable development goals (SDGs), particularly SDG 12.
Keywords: fly ash, zeolite, NaA, pelletization.

INTRODUCTION

Agro-industrial wastes and by-products are eco-friendly adsorbents because they are locally available and low-cost sources for water and wastewater treatment applications [1, 2]. Many materials can be used as low-cost adsorbents, such as rice straw and husks rice straw [3], raw/activated sawdust [4, 5], diatomaceous earth [6], and sugarcane bagasse [7-10]. The amount of solid waste residue produced by coal-fired power plants has been steadily increasing around the world. Coal ash production is currently expected to be over 600 million ton per year worldwide, with fly ash accounting for roughly 500 million ton per year, or 75-80% of total ash produced [11]. The production of zeolites from coal fly ash can be done by means of different hydrothermal activation methods [12-14]. The synthesis methods include direct hydrothermal, two-step hydrothermal, alkaline fusion-assisted hydrothermal, microwave-assisted methods, molten salt, solvent-free method, and ultrasonic-assisted method [15-20]. We focus on zeolitic materials because they possess a large surface area and a net negative charge which lead to a high adsorption capacity due to their channel structure, which allows them to easily attract heavy metals and cationic dyes. Besides, they are more cost-effective due to the low cost and abundance of minerals that act as good cation exchangers [16, 19].

High purity NaA zeolite can be obtained through a two-step process consisting of a fusion of the mixture of fly ash and alkali and adding of an external source of aluminate in the first stage. In the second stage, the alkali melt product is processed through hydrothermal treatment. On completion of the synthesis process, fly ash zeolite is obtained in the form of powder [11, 21-23]. In liquid-phase applications, both granular and powdered zeolites can be employed. The granular form can be employed in a fixed-bed column and is regenerable, but the powdered form is typically utilized in batch processes, without regeneration. Furthermore, due to technical issues such as a significant drop in pressure, diffusion limits, hydraulic resistance, clogging in packed beds, and the danger of losing a bed, powdered materials are unsuitable for many industrial processes (for example, gas adsorption and catalysis). Therefore, depending on the application, a pelletization process is necessary to perform. The two types of the pelletization process are dry granulation and wet granulation. In the dry granulation process, the powder particles are intensively mixed and aggregated under high pressure resulting in a considerable size enlargement. The wet granulation involves the addition of a liquid solution (with or without binder) to the powder sample to promote liquid dispersion and granule growth.

It is known that pure zeolite powder does not exhibit binding properties so an appropriate binder is needed to form pellets [24]. The most common binders are clays (bentonite, kaolinite, attapulgite, boehmite), synthetic binders (alumina, silica), or combinations of these materials. The wet granulation process is commonly used for manufacturing binder-containing zeolite with the addition of water in order to adjust the viscosity and plasticity of the mixture [25,

* https://orcid.org/0000-0003-1618-0264

26]. Several studies have demonstrated the use of clays as an inorganic binder in zeolite pellets [27-33]. The type and amount of the binder can affect the mechanical durability of the granulate and also the sorption capacity of the granulated material. In the present work, fly ash-based zeolite NaA powder, bentonite, and kaolinite as well as a combination of bentonite with kaolinite were considered in the pelletization process. The content of NaA zeolite powder was fixed at 90% by mass (minimum) in all applied methods so that the greatest possible amount of material containing coal fly ash was used.

MATERIALS AND METHODS

Materials: all chemicals used for experimental studies were of analytical grade. A coal fly ash sample was collected in the Thermoelectric Complex Jorge Lacerda, located in Santa Catarina State, Brazil. Bentonite and kaolinite used as a binder in this study were commercially produced materials. Sodium hydroxide (97%) and sodium aluminate (50-56%) obtained from Sigma-Aldrich were used in the preparation of zeolite synthesis.

NaA zeolite powder synthesis: firstly, 10 g of coal fly ash was mixed with NaOH at a 1:1.2 (wt%) ratio. The mixture was heated at 500 ºC for 1 h. After cooling at room temperature, commercial sodium aluminate was added to the ground mixture to control the molar ratio (SiO_2/Al_2O_3=1) and mixed with 100 mL of deionized water. The mixture was then stirred at room temperature for 16 h and heated at 100 °C for 7 h. After cooled at room temperature, the suspension was filtered and the solid was repeatedly washed with 1 L of deionized water and dried at 105 °C for 16 h. Zeolite A synthesized in powder form was named ZAP [22].

Preparation of NaA granules: after tests with several types of binders, preliminary results indicated that bentonite, kaolinite, and the mixture of the two clays presented the best characteristics for the pelletizing process [34]. To prepare the NaA granules, ZAP was mixed with a binder (bentonite, kaolinite, or bentonite+kaolinite) and homogenized. Then, deionized water, with a ratio of dry mixture mass:volume=1:1, was slowly poured into a cavity in the center of the container containing the dry mixture until a paste was obtained. After homogenization, the pasty mixture was molded into spherical granules (TR04, Eirich).

Table I - Composition (wt%) of binders used in pelleting of NaA zeolite powder.

Zeolite granular sample	Bentonite	Kaolinite
ZAG1	5	5
ZAG2	8	2
ZAG3	10	0
ZAG4	0	10
ZAG5	5	0
ZAG6	4	1

After the molding step, the material was dried in an oven at 100 °C for 2 h and calcined in a muffle at 500 °C for 2 h. The diameters of granules ranged between 3 and 6 mm. ZAP zeolite content was maintained at 90 and 95 wt%. Bentonite, kaolinite, and a mixture of the two binders were assessed with different amounts shown in Table I, and samples were named ZAG1 to ZAG6.

Characterization of materials: physicochemical properties of coal fly ash have been reported in previous studies [34, 35]. The mineralogical compositions were determined by X-ray diffraction (XRD), with a diffractometer (Miniflex 2, Rigaku) using CoKα radiation at 40 kV and 20 mA over the range (2θ) of 5-80° with a scan speed of 0.5 °.min^{-1}. The degree of purity was estimated using the reference intensity ratio (RIR) method. The chemical composition was determined by X-ray fluorescence spectroscopy (XRF, RIX-3000, Rigaku). Thermal analysis was performed by thermogravimetry (TGA/SDTA 851, Mettler-Toledo). Each sample (~10 mg) was heated from 25 to 1000 °C at a heating rate of 10 °C.min^{-1} under an oxygen flux (50 mL.min^{-1}). The scanning electron micrographs were obtained using a microscope (Quanta FEG 650, FEI). Some samples were embedded in epoxy resin, cut, and polished to perform the back-scattered electron (BSE) imaging and energy dispersive spectroscopy (EDS) mapping analysis. Vibration spectra of the samples were determined by Fourier transform infrared spectroscopy (FTIR, Frontier, Perkin Elmer) within a wavenumber from 4000 to 400 cm^{-1}. Textural properties of the samples were measured from N_2 adsorption/desorption isotherms at 77 K (TriStar II 3020, Micromeritics). The samples were purged with nitrogen gas for 12 h at 150 ºC. The specific surface area was calculated by the Brunauer-Emmet-Teller (BET) method [36], and the microporous surface area, external surface area, and micropore volume were evaluated by the t-plot method [37], the pore diameter and mesopore volume were obtained by the Barrett-Joyner-Halenda (BJH) method. The pore-size distribution was calculated by analyzing both the adsorption and desorption branches of the isotherm using the BJH method [38]. Cation exchange capacity was determined by a previously described procedure [22]. The stability in water of the granular zeolite was determined by weighing the pellet mass before and after the cation exchange capacity test. Workability was related to the ease of handling and molding the paste consisting of powdered zeolite, binder, and water to form pellets. All tests were done in triplicates. The drop test consisted of dropping the material from a height of 100 cm onto a metallic surface and recording the number of drops each granule withstood until it disintegrated [39]. The compressive strength test was performed for the samples which were selected in the drop test. A texturometer (TA. XT.Plus, Stable Micro Systems) was used. The test was carried out at room temperature, using a 500 N load cell and a constant velocity of 0.02 mm.s^{-1}, until the primary fracture (F_F). The tests were repeated 5 times per series of samples. The characteristic fracture strength (σ_F) was

calculated from the ratio of the fracture force (F_F) related to the cross-sectional area (A) of the granule [40]:

$$\sigma_f = \frac{F_F}{A} = \frac{F_F}{\pi R^2} \quad (A)$$

RESULTS AND DISCUSSION

Characterization of powdered synthesis product: the chemical constituents of zeolite obtained from the X-ray fluorescence technique (XRF) are shown in Table II. It can be observed that the major constituents were SiO_2, Al_2O_3, Na_2O, CaO, and Fe_2O_3. Oxides of titanium, potassium, magnesium, and others were found in amounts below 0.8 wt%. The molar ratio of Si to Al in the synthesized zeolite was 1.0 within the range of zeolite A reported in the literature, i.e. 0.7 to 1.2 [41]. The crystalline phase identified in the zeolite synthesized ZAP was zeolite NaA (JCPDS 43-0142) as the predominant phase (Fig. 1). The degree of purity was calculated at 97.0%. It is worth mentioning that the quartz phase (JCPDS 33-1161) came from the fly ash as it is a stable phase [42]. The morphology of synthesized NaA is shown in Figs. 2a and 2b. The cube-shaped crystals of zeolite were observed in addition to amorphous-looking material from raw materials used in the synthesis. The crystals were 1 μm in size (Fig. 2b). The cubic morphology indicated crystallization of the LTA phase having Si/Al ~1 [43].

The profile of the thermogravimetric curve of ZAP is shown in Fig. 3. From the thermographs, the great loss of mass associated with the loss of free and physically adsorbed water inside the zeolite pores occurred between 32.44 and 255.49 °C (15.04%). It can be seen that the sample showed continuous weight loss until 400 °C due to dehydration, after that it became almost constant. In the second stage, the mass loss between 255.49 and 677.62 °C (4.48%) can be attributed to the decomposition of $CaCO_3$ from fly ash used as raw material for the zeolite synthesis [44]. The maximum weight loss of water from ZAP (19.52%) was comparable with the values found for the 4A commercial zeolite, which is approximately 20% [44-46].

FTIR spectroscopy was used to confirm the structure of the synthesized Na-A sample, as shown in Fig. 4. FTIR bands at 463, 554, 663, 1002, 1649, and 3430 cm^{-1} were observed. The band at 463 cm^{-1} was ascribed to the internal vibration of T-O (T= Si, Al) bending. The band at 554 cm^{-1} was associated with the external vibration of double four-rings of the NaA zeolite framework [47]. The band at 663 cm^{-1} was attributed to the internal vibration of T-O symmetric stretching. The band at 1002 cm^{-1}, related to the internal vibration of T-O asymmetric stretching, is a major feature in the framework of zeolite 4A [11]. The band observed

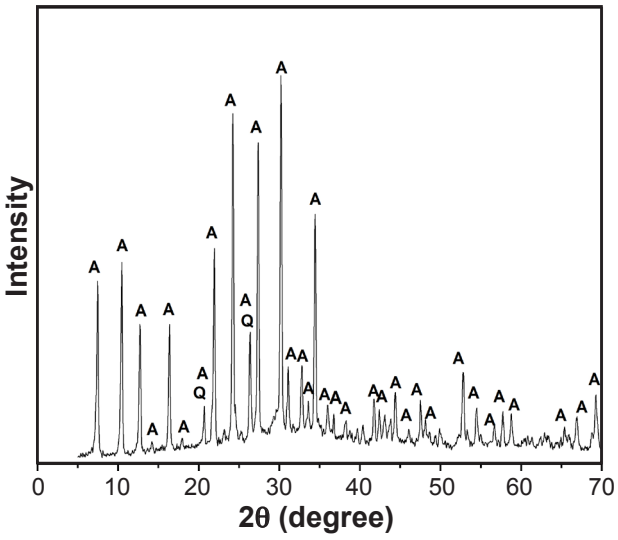

Figure 1: XRD pattern of zeolitic material synthesized from coal ash (Q: quartz, A: NaA zeolite).

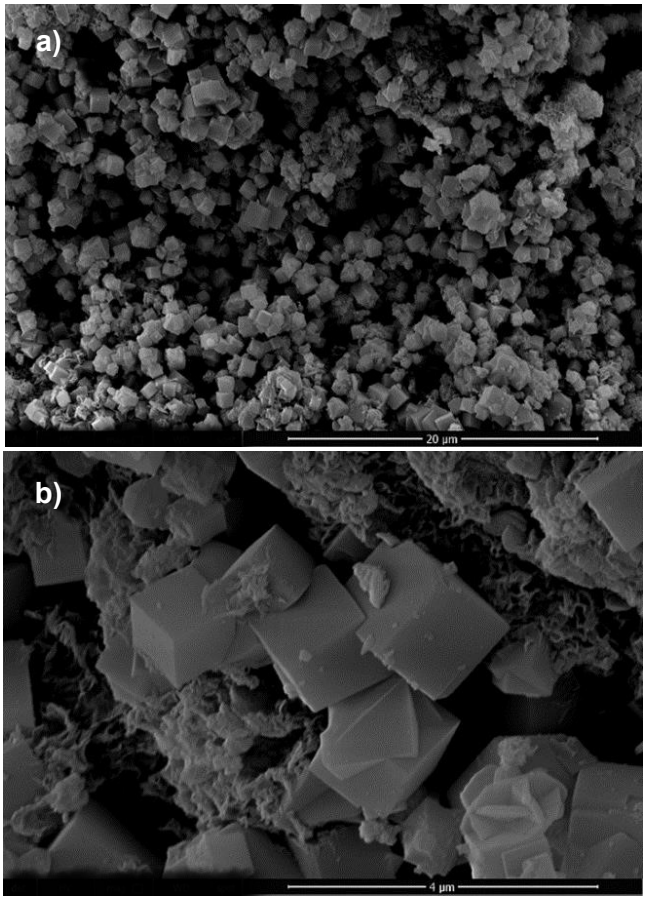

Figure 2: SEM micrographs of zeolite ZAP at different magnifications.

Table II - Chemical composition (wt%) of the major oxides in ZAP.

SiO_2	Al_2O_3	Na_2O	CaO	Fe_2O_3	TiO_2	K_2O	MgO	SO_3	ZrO_2	P_2O_5	MnO	ZnO	Others	LOI[1]
31.3	24.2	13.8	5.40	3.57	0.758	0.694	0.447	0.071	0.031	0.026	0.022	0.021	<0.001	19.6

[1]: *loss on ignition*.

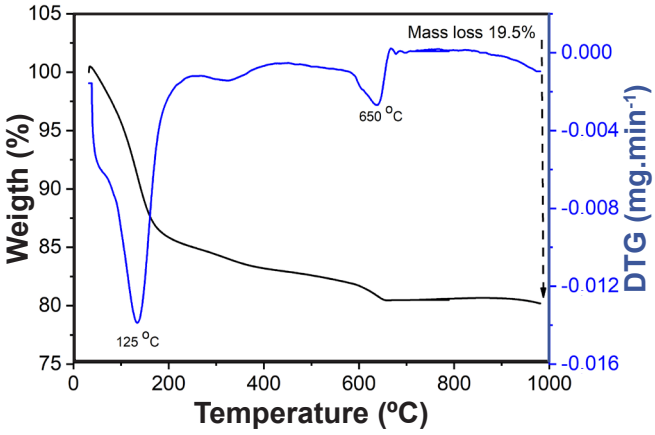

Figure 3: Thermogravimetry (TG) and derivative thermogravimetry (DTG) curves of ZAP.

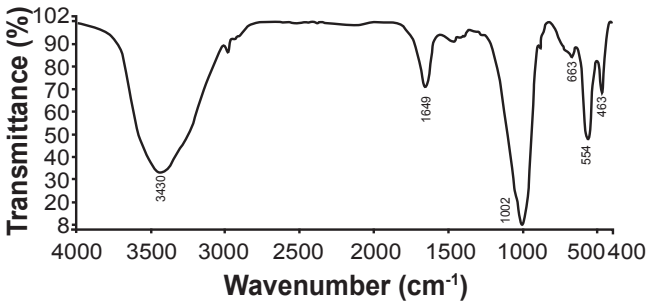

Figure 4: FTIR spectrum of synthesized zeolite ZAP.

at 1649 cm^{-1} corresponded to the H-OH deformation and usually is evidence of the presence of hydrated compounds whose water is strongly linked to the molecular structure of the compound. The band at 3430 cm^{-1} is characteristic of OH hydrogen bonded to the oxygen ions of the zeolite framework [48]. Therefore, it can be concluded that the structural units of the synthesized zeolite A were similar to those reported in the literature [49-51].

The nitrogen adsorption/desorption isotherm of the prepared zeolite is given in Fig. 5a. The isotherm could be classified as type IV according to the IUPAC standard [52]. The isotherm showed ascending adsorption at p/p_0 <0.2 which can be attributed to adsorption in micropores. The shape of the

Table III - Chemical composition (wt%) of bentonite and kaolinite.

Oxide	Bentonite	Kaolinite
SiO_2	51.4	47.4
Al_2O_3	15.0	34.8
Fe_2O_3	9.82	1.27
MgO	2.24	<0.001
CaO	1.74	<0.001
Na_2O	1.42	0.120
TiO_2	1.40	1.15
K_2O	0.579	0.041
Cl	0.180	0.060
V_2O_5	0.042	<0.001
BaO	0.036	<0.001
MnO	0.033	<0.001
P_2O_5	0.032	0.127
Cr_2O_3	0.021	<0.001
SrO	0.019	0.017
ZnO	0.019	<0.001
NiO	0.013	0.009
Rb_2O	0.007	<0.001
Nb_2O_2	0.005	<0.001
SO_3	<0.001	0.230
CuO	<0.001	0.009
PbO	<0.001	0.019
Ga_2O_3	<0.001	0.010
Loss on ignition	16.0	14.7

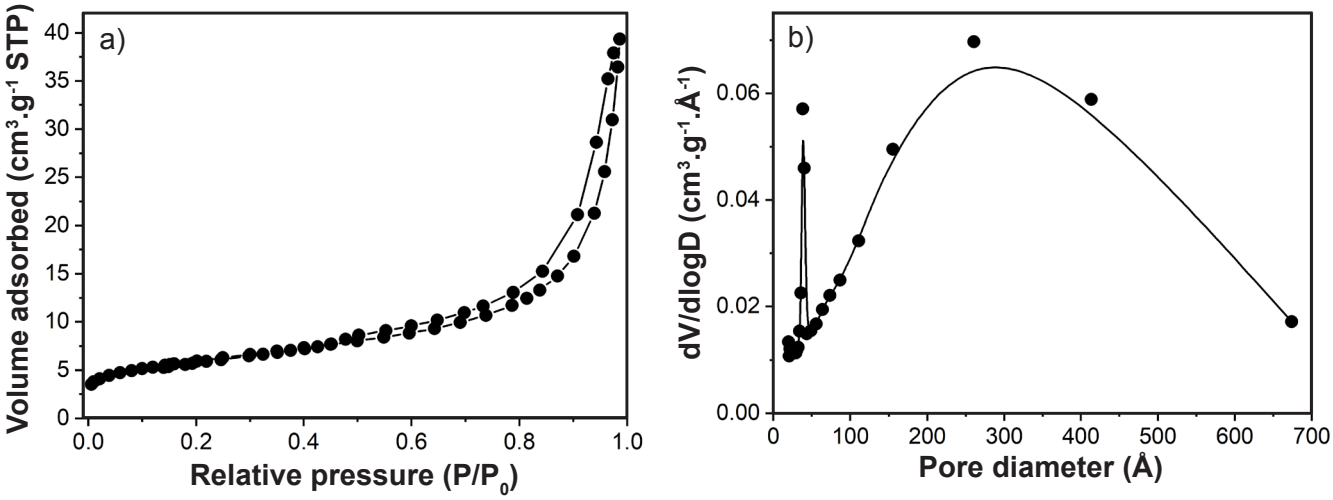

Figure 5: Nitrogen adsorption-desorption isotherm (a) and pore diameter distribution curve (b) for ZAP.

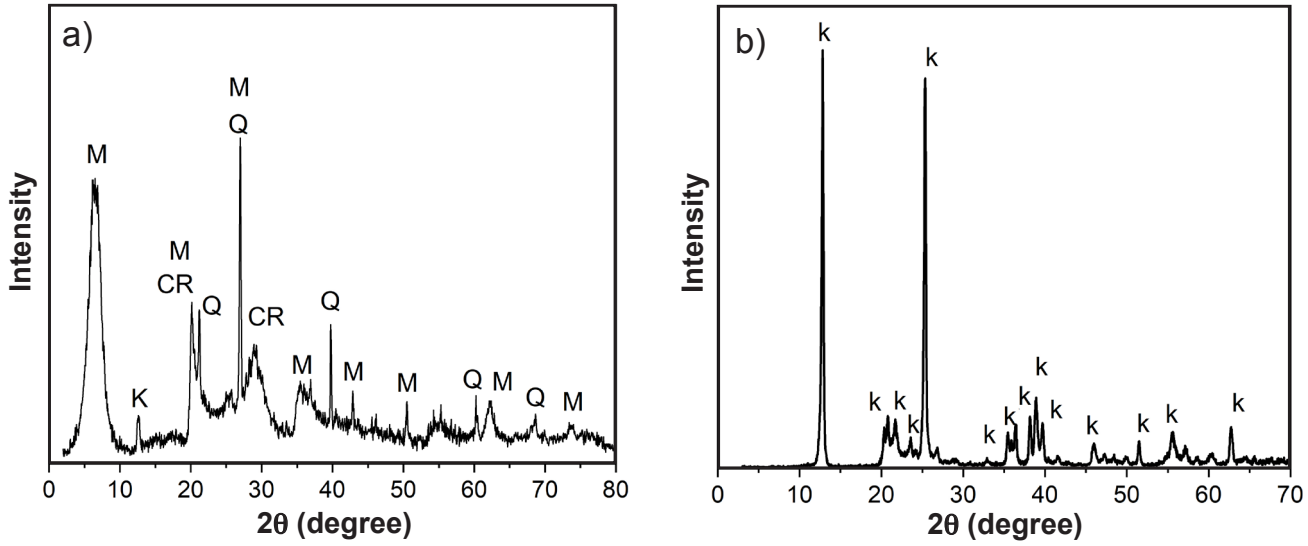

Figure 6: XRD patterns of: a) bentonite (M: montmorillonite, Q: quartz, k: kaolinite, CR: cristobalite); and b) kaolinite (k: kaolinite).

hysteresis loop was in accordance with the H3 type of IUPAC classification, usually associated with slit-shaped mesoporous formed by platelet aggregation resulting in large pore size distribution. The surface area and the pore volume were 20.94 $m^2.g^{-1}$ and 0.06178 $cm^3.g^{-1}$, respectively. Fig. 5b shows the BJH pore size distribution curve of the as-synthesized zeolite. A bimodal pore size distribution was observed mainly due to the presence of mesopore centered around 50 and 280 Å. The distribution of pores above 500 Å indicated the presence of macropores.

Characterization of binders: the chemical compositions of bentonite and kaolinite are given in Table III. An analysis of the results indicated that both clays had high SiO_2 (~50%) and Al_2O_3 (15-35%) contents. Bentonite presented ~10% of Fe_2O_3 content and MgO, CaO, Na_2O, and TiO_2 in the range of 1.4% to 2.2%. The Fe_2O_3 and TiO_2 contents were relatively low (<1.3%) for kaolinite. These oxides are mainly associated with bentonite and kaolinite structures. The X-ray diffraction patterns of used materials are illustrated in Fig. 6. The bentonite (Fig. 6a) contained mainly montmorillonite. In addition, quartz, cristobalite, and kaolinite were also identified at low amounts. The XRD pattern in Fig. 6b indicated a clay with a high degree of purity presenting a well-defined and intense peak for kaolinite in its characteristic angle (~14° 2θ, CoKα), which refers to the distance between planes (001) of the monoclinic structure, with the characteristic basal reflection of 7.09 Å (d_{001}) [53].

Evaluation of the produced granular zeolites: important characteristics of the six granular zeolites are listed in Table IV. The investigated properties included workability, drop resistance, water stability, and cation exchange capacity values. The pellets from the stoichiometric mixture contained 90 or 95 wt% zeolite. The structure of ZAG1, ZAG4, and ZAG6 samples collapsed. The best results were obtained with ZAG2, ZAG3, and ZAG5 samples. These granules were the most resistant and showed similar cationic exchange capacity values to the value obtained with zeolite A in the powder form (ZAP).

The deformation and the breakage behavior of granulate samples were described by force-displacement curves. The force-displacement curves for ZAG2, ZAG3, and ZAG5 samples presented similar behavior (Fig. 7). At the beginning of the stressing, small elastic deformation was

Table IV - Characteristics of granular zeolites with different binders.

Sample	Binder (wt%)		Workability[1]	Drop test[2]	Pellet water stability[1]	CEC[3] ($meq.g^{-1}$)
	Bentonite	Kaolinite				
ZAG1	5	5	L	13	L	Collapsed
ZAG2	8	2	M	40	H	3.9
ZAG3	10	0	H	51	H	3.9
ZAG4	0	10	L	1	Collapsed	-
ZAG5	5	0	M	36	H	3.5
ZAG6	4	1	L	10	L	Collapsed
ZAP	0	0	-	-	-	3.8

[1]: L=low, M=medium, H=high; [2]: number of drops without breaking the pellets; [3]: cation exchange capacity.

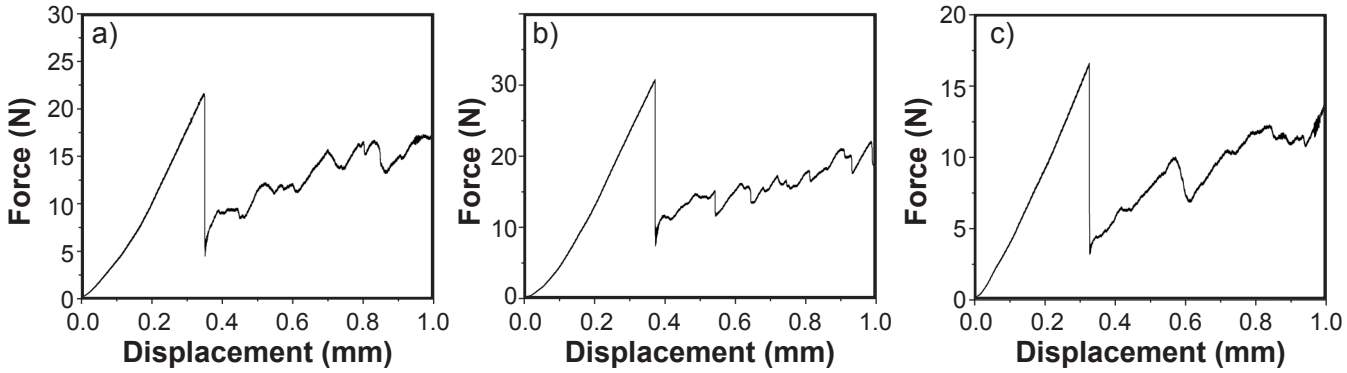

Figure 7: Force-displacement curve of: a) ZAG2; b) ZAG3; and c) ZAG5.

observed (linear curve up to ~0.1 mm). When the curve deviated from the linear trend, a considerable elastic-plastic deformation before primary breakage occurred. After the primary breakage point, the multiple stressing leads to the failure of the fragments. Therefore, samples exhibited dominant elastic-plastic properties. Similar mechanical behavior during compression was observed with commercial synthetic zeolitic molecular sieves of type 4A in the form of granules [40, 54, 55]. The average values of mechanical properties are summarized for examined granulates in Table V. The pellet prepared with 90 wt% zeolite and 10 wt% bentonite exhibited the highest fracture strength and breakage force. During the shaping process, the elevated temperature induced strong bonds between the binder and the porous powder particles and between the porous powder particles themselves. Also, a secondary pore system was created consisting of mesopores and/or macropores [33, 56, 57]. The increase in bentonite content increased strength due to improvement in the interaction between the zeolite particles. The decrease in compressive strength with increasing kaolinite content can be attributed to an increase in secondary pore dimensions and heterogeneous distribution. This negative influence of kaolinite on the mechanical strength of pellets was also observed in a previous study [32]. The authors produced pellets with different amounts of commercial zeolite, bentonite, and kaolin in the form of the Raschig ring. Therefore, a sample with the mentioned composition of 90 wt% zeolite and 10 wt% bentonite (ZAG3) was selected as optimum granular zeolite A, which was characterized by different complementary techniques.

Table V - Macroscopic mechanical properties of the granule samples.

Sample	Binder (wt%)		Breakage force (N)	Fracture strength (MPa)
	Bentonite	Kaolinite		
ZAG2	8	2	24.0	1.9
ZAG3	10	0	32.7	2.9
ZAG5	5	0	17.0	0.9

Characterization of granular synthesis product ZAG3: the chemical composition of the granular zeolite is reported in Table VI, along with the SiO_2/Al_2O_3 ratio. An increase of silica and alumina in the chemical composition of the zeolite after pelletization compared to power zeolite (Table II) was confirmed since these were the main constituents of the binding agent used in the process. The X-ray diffraction patterns of synthetic zeolitic materials in powder and granular forms are illustrated in Fig. 8. The pelletizing process had no effect on the crystallinity of the powder zeolite, as evidenced by X-ray diffraction. No new diffraction peaks were observed, indicating no new crystalline phase formation, which is important to maintain the zeolite properties. The reduced intensities observed for the granules in relation

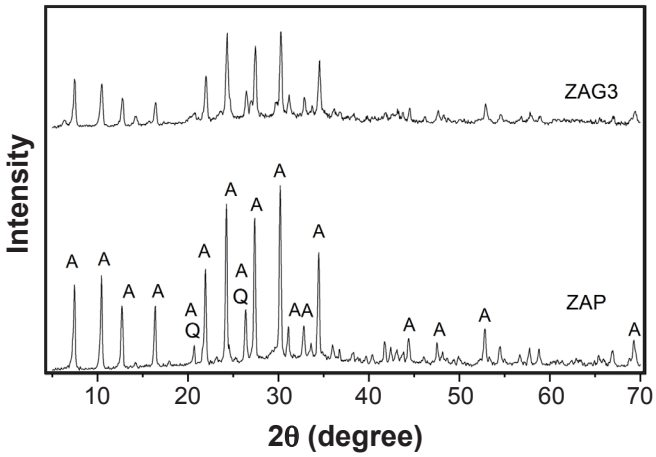

Figure 8: XRD patterns of power zeolite and granular zeolite (Q: quartz, A: NaA zeolite).

Table VI - Chemical composition (wt%) of the major oxides of ZAG3.

SiO_2	Al_2O_3	Na_2O	Fe_2O_3	CaO	MgO	TiO_2	K_2O	SO_3	P_2O_5	MnO	ZnO	SiO_2/Al_2O_3	LOI[1]
41.5	28.3	15.4	5.77	5.67	1.10	1.01	0.685	0.202	0.045	0.028	0.021	1.47	17.3

[1]: *loss on ignition*.

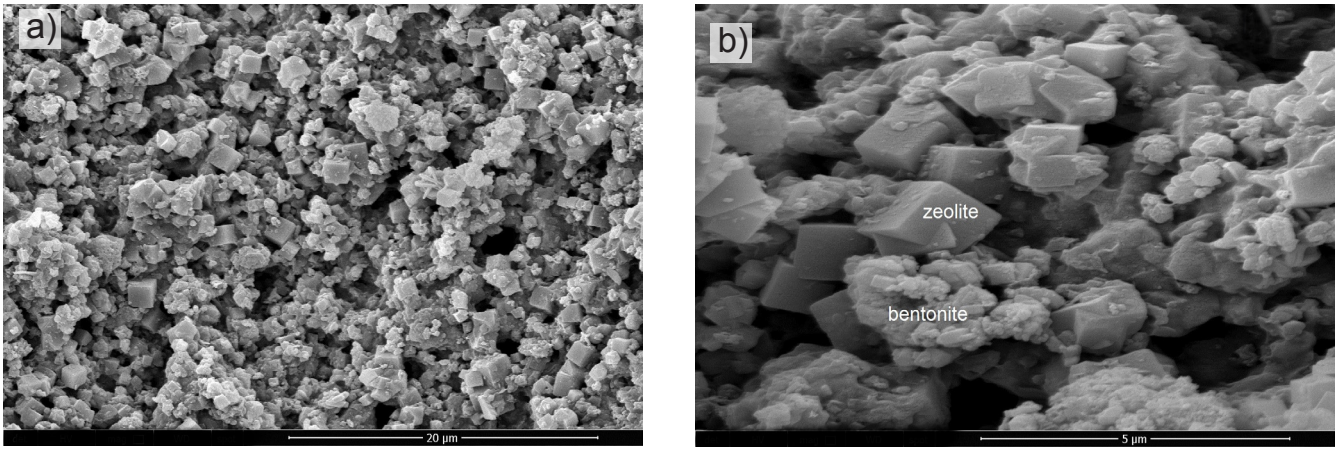

Figure 9: SEM micrographs of granular zeolite ZAG3 at different magnifications.

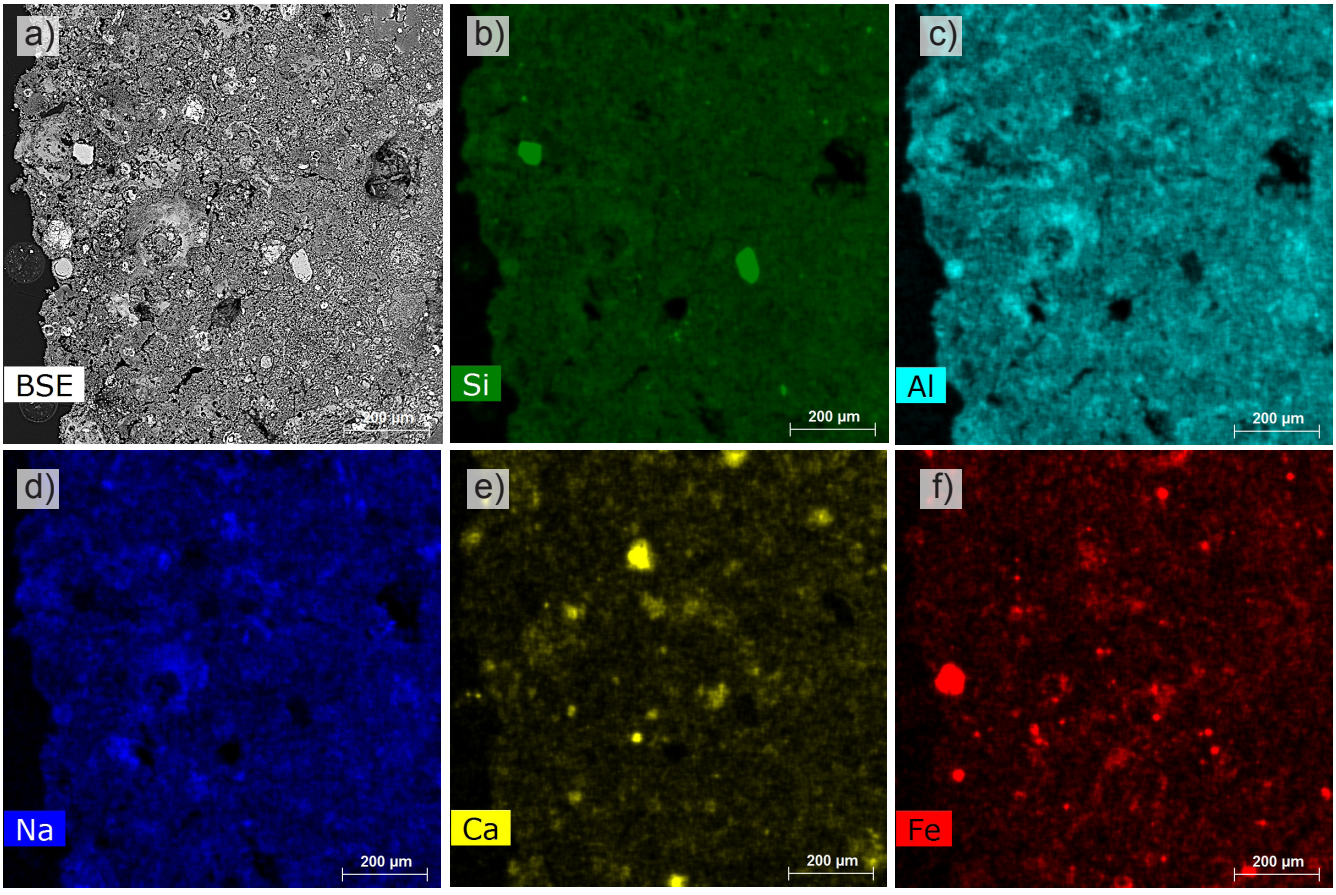

Figure 10: SEM (BSE) image and elementary distribution maps of an internal cross-section of the granular zeolite ZAG3.

to the powder material resulted from the inclusion of the bentonite. This decrease in reflection intensity was also observed in the diffractogram of ZSM-5 zeolite granular prepared using attapulgite as a clay binder [58].

Fig. 9 shows the micrographs obtained from the granular zeolite. Zeolite NaA crystals with a well-defined cubic shape were observed demonstrating that there was no change in the structure during the pelleting process. The zeolite particles surrounded by the binder (bentonite) were clearly visible. The surface elemental distribution of granular zeolite was examined by EDS mapping. Fig. 10 shows images that confirmed the predominance of the elements Si, Al, Na, Ca, and Fe, in agreement with the chemical composition (Table VI). Ca and Fe were elements of unreacted ash present in the zeolite sample.

Fourier transform infrared spectroscopy (FTIR) analysis was relevant to complement the study on the interaction between the active groups of zeolite and the binding agent used in the pelletization process. FTIR spectrum was recorded in the 400-4000 cm^{-1} region (Fig. 11). The main

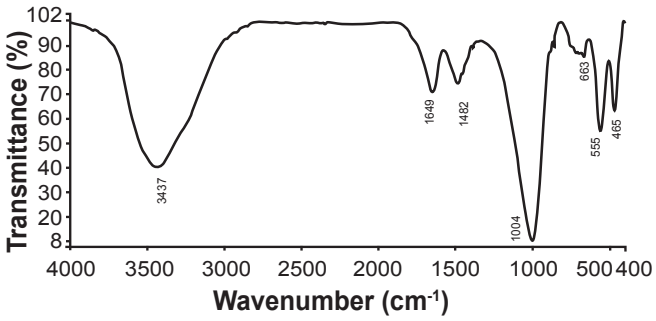

Figure 11: FTIR spectrum of granular zeolite ZAG3.

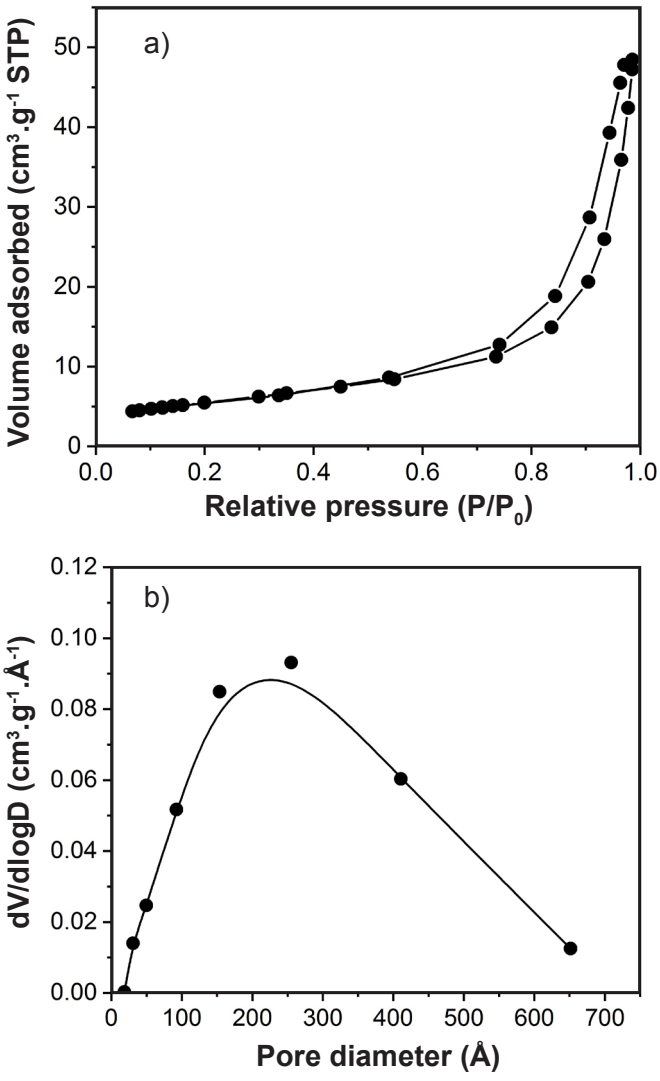

Figure 12: Nitrogen adsorption-desorption isotherm (a) and pore diameter distribution curve (b) for ZAG3.

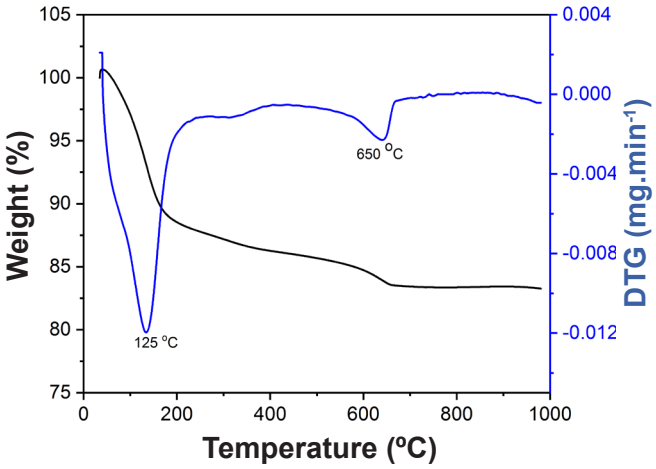

Figure 13: TG and DTG curves of ZAG3.

bands of powdered zeolite were observed in the spectrum of pelleted zeolite: the presence of H_2O and hydroxyls (3437, 1649 cm^{-1}); alumina present in the pores (1482 cm^{-1}); stretching vibration modes of Si-O and Al-O tetrahedra (1004, 663 cm^{-1}); external vibration of double-rings (555 cm^{-1}); and bending modes of T-O-T bridges (465 cm^{-1}). This information is further evidence of the preservation of the structure of zeolites after the pelletization process.

From Fig. 12a, it can be inferred that the 4A granular zeolite showed mesoporosity characteristics as it was evident on the adsorption/desorption isotherm, similar to the adsorption/desorption isotherm of zeolite A powder (Fig. 5a). Also, the adsorption in p/p_0 <0.05 is the characteristic of micropores. Fig. 12b shows the corresponding pore diameter distribution curve of the NaA granular zeolite. The pore sizes of the sample were concentrated in the 50-650 Å range. For zeolite powder, the distribution was bimodal with a major peak at ~280 Å and a minor peak at around 50 Å (Fig. 5b). ZAG3 showed a unimodal distribution with a peak of around 270 Å. Probably, the presence of binder in the structure of the granules resulted in the blocking of pores of smaller diameters in the zeolite. The BET, t-plot, and BJH methods were employed to calculate the textural properties of synthesized zeolites before (ZAP) and after (ZAG3) the addition of a binder to the conformation of the samples into spherical shapes. As shown in Table VII, the values of zeolite A powder and pellet were similar, with the exception of the micropore volume as indicated in the pore diameter distribution curve.

Thermogravimetric analysis was performed to confirm the thermal stability of the pelleted zeolite (Fig. 13). The profile of the thermogravimetric curves of the granular

Table VII - Textural properties of ZAP and ZAG3.

Sample	S_{BET} [1] ($m^2.g^{-1}$)	S_{Micro} [2] ($m^2.g^{-1}$)	S_{exter} [3] ($m^2.g^{-1}$)	V_{Micro} [4] ($cm^3.g^{-1}$)	D_{poro} [5] (Å)	V_{Meso} [6] ($cm^3.g^{-1}$)
ZAP	20.94	3.177	17.77	0.001427	119.9	0.06178
ZGP3	19.69	2.203	17.40	0.000843	128.9	0.07537

[1]: BET specific surface area; [2]: microporous surface area; [3]: external surface area; [4]: micropore volume; [5]: pore diameter, [6]: mesopore volume.

zeolite was maintained in relation to that obtained for the powdered zeolite (Fig. 3), thus confirming the thermal stability of the material after the pelletization process. For both granular and powder zeolites, there was the elimination of the adsorbed water in the temperature range of approximately 50 to 200 °C in the first stage. Additionally, in the second stage (650 °C), the TG curve showed a mass loss corresponding to the presence of a small amount of $CaCO_3$ in the ashes remaining from the synthesis process.

CONCLUSIONS

NaA-type zeolite powder was prepared from fly ash through fusion followed by hydrothermal treatment. The XRF, XRD, and SEM proved that the synthesized zeolite presented high purity. For the granulation of zeolite, we used two types of inorganic binders (bentonite and kaolinite) and granular samples were prepared with six different concentrations of binding agents (5-10 wt%) by applying the wet granulation method. The drop number of pellets was determined from a height of 100 cm. The elastic-plastic compression behavior of granulates and characteristic parameters (breakage force and fracture strength) were described by means of force-displacement curves. The NaA granules exhibited both elastic and elastic-plastic behavior with dominant elastic-plastic properties. Kaolinite did not show the expected features of the binder, while the use of bentonite as a binder was acceptable from the viewpoint of the granule strength property. The best results for the mechanical properties were obtained with the composition prepared with 90 wt% zeolite and 10 wt% bentonite. The maximum force required to break granules was 32.7 N and the fracture strength of the pellet was 2.9 MPa. The favorable physicochemical characteristics of the NaA zeolite powder remained intact in the granulated form. Furthermore, the granules prepared with bentonite exhibited satisfactory ion exchange capacity. In final remarks, it was concluded that fly ash could be converted into a value-added product, minimizing the environmental impact of disposal problems. The NaA zeolite in granular form has the potential to be used as adsorbents for the removal of pollutants from wastewater at the thermoelectric plant itself. In this approach, the adoption of the circular economy in waste management contributes significantly to the achievement of the sustainable development goals (SDGs), specifically, SDG 12: "by 2030, substantially reduce waste generation through prevention, reduction, recycling, and reuse".

ACKNOWLEDGMENTS

The authors are grateful to Conselho Nacional de Desenvolvimento Científico e Tecnológico (CNPq) and Coordenação de Aperfeiçoamento de Pessoal de Nível Superior (CAPES) for supporting this study and Jorge Lacerda coal-fired power plant for providing coal ash sample.

REFERENCES

[1] E. Matei, M. Râpa, A.M. Predescu, A.A. Turcanu, R. Vidu, C. Predescu, C. Bobirica, L. Bobirica, C. Orbeci, Materials **14** (2021) 458.
[2] N. Hossain, M.A. Bhuiyan, B.K. Pramanik, S. Nizamuddin, G. Griffin, J. Clean. Prod. **255** (2020) 120261.
[3] B.A. Goodman, J. Bioresour. Bioprod. **5** (2020) 143.
[4] S. Benyoucef, D. Harrache, S. Djaroud, K. Sail, D. Gallart-Mateu, M. de la Guardia, Cellulose **27** (2020) 8169.
[5] N.U. Rahman, I. Ullah, S. Alam, M.S. Khan, L.A. Shah, I. Zekker, J. Burlakovs, A. Kallistova, N. Pimenov, Z. Vincevica-Gaile, Y. Jani, M. Zahoor, Water **13** (2021) 2136.
[6] M.A. Semião, C.W.I. Haminiuk, G.M. Maciel, J. Environ. Chem. Eng. **8** (2020) 103617.
[7] W.K.O.C. Costa, S. Gavazza, M.M.M.B. Duarte, S.K.B. Freitas, N.T.G. Paula, A.P.S. Paim, Water Air Soil Pollut. **232** (2021) 358.
[8] V. Yadav, J. Ali, M.C. Garg, J. Hazard. Toxic Radioact. Waste **25** (2021) 4020067
[9] S. Rovani, J.J. Santos, P. Corio, D.A. Fungaro, J. Braz. Chem. Soc. **30** (2019) 1524.
[10] S. Rovani, J.J. Santos, P. Corio, D.A. Fungaro, ACS Omega **3** (2018) 2618.
[11] A. Iqbal, H. Sattar, R. Haider, S. Munir, J. Clean. Prod. **219** (2019) 258.
[12] P. Rybowicz, A. Kowalczyk, A. Łagosz, M. Michalik, A. Adamski, Sustain. Chem. Pharm. **27** (2022) 100637.
[13] P. Kunecki, R. Panek, M. Wdowin, T. Bień, W. Franus, Int. J. Coal Sci. Technol. **8** (2021) 291.
[14] P. Kunecki, R. Panek, A. Koteja, W. Franus, Microporous Mesoporous Mater. **226** (2018) 102.
[15] X.-Y. Zhang, C.-Q. Li, S.-L. Zheng, Y.-H. Di, Z.-M. Sun, Int. J. Miner. Metall. Mater. **29** (2022) 1
[16] D. Azizi, F. Ibsaine, J. Dionne, L.-C. Pasquier, L. Coudert, J.-F. Blais, Microporous Mesoporous Mater. **318** (2021) 111029.
[17] X. Ren, R. Qu, S. Liu, H. Zhao, W. Wu, H. Song, C. Zheng, X. Wu, X. Gao, Aerosol Air Qual. Res. **20** (2020) 1127.
[18] M. Harja, G. Ciobanu, in "Handbook of nanomaterials and nanocomposites for energy and environmental applications", O. Kharissova, L. Martínez, B. Kharisov (Eds.), Springer (2020) 1.
[19] A. Khaleque, Md.M. Alam, M. Hoque, S. Mondal, J.B. Haider, B. Xu, M.A.H. Johir, A.K. Karmakar, J.L. Zhou, M.B. Ahmed, M.A. Moni, Environ. Adv. **2** (2020) 100019.
[20] T. Paramitha, Adv. Eng. Res. **198** (2020) 407.
[21] J. Izidoro, D. Castanho, C. Rossati, D. Fungaro, S. Guilhen, T. Nogueira, M.F. Andrade, Int. J. Environ. Imp. **2** (2019) 215.
[22] J.C. Izidoro, D.A. Fungaro, J.E. Abbott, S. Wang, Fuel **103** (2013) 827.
[23] B.C. Amoni, A.D.L. Freitas, R.A. Bessa, C.P. Oliveira, M. Bastos-Neto, D.C.S. Azevedo, S.M.P. Lucena, J.M. Sasaki, J.B. Soares, S.A. Soares, A.R. Loiola, Mater. Chem. Phys. **275** (2022) 12519.

[24] R. Panek, M. Wdowin, L. Bandura, E. Wisła-Walsh, P. Gara, Mineralogia **48** (2017) 3.
[25] R. Bingre, B. Louis, P. Nguyen, Catalysts **8** (2018) 163.
[26] K. Gleichmann, B. Unger, A. Brandt, in "Zeolites", C. Belviso (Ed.), IntechOpen (2016) 89.
[27] T.F. Aquino, S.T. Estevam, V.O. Viola, C.R.M. Marques, F.L. Zancan, L.B. Vasconcelos, H.G. Riella, M.J.R. Pires, R. Morales-Ospino, A.E.B. Torres, M. Bastos-Neto, C.L. Cavalcante Jr., Fuel **276** (2020) 118143.
[28] N. Czuma, R. Panek, P. Baran, K. Zarębska, Clay Miner. **55** (2020) 40.
[29] S.B. Ainun, R. Kugaann, M.F Chow, Int. J. Eng. Technol. **7** (2018) 333.
[30] A.L. Ciosek, G.K. Luk, Int. J. Environ. Pollut. Rem. **2** (2014) 96.
[31] A.L. Alaica, "On-site total phosphorus removal from wastewater", M.Sc., Ryerson Un., Toronto (2012).
[32] A. Salem, R.A. Sene, Chem. Eng. J. **174** (2011) 619.
[33] R.V. Jasra, B. Tyagi, Y.M. Badheka, V.N. Choudary, T.S.G. Bhat, Ind. Eng. Chem. Res. **42** (2003) 3263.
[34] T.C.R. Bertolini, "Synthesis and characterization of zeolitic material granular of coal ash and evaluation in the application as adsorbent", Dr. Thesis, Inst. Pesq. Energ. Nucl., S. Paulo (2019).
[35] T.C.R. Bertolini, S.N. Guilhen, D.A. Fungaro, in "Fly ash: properties, analysis and performance", J. Parker (Ed.), Nova Sci. Publ. (2017) 195.
[36] S. Brunauer, P.H. Emmett, E. Teller, J. Am. Chem. Soc. **60** (1938) 309.
[37] W.D. Harkins, G. Jura, J. Am. Chem. Soc. **66** (1944) 1366.
[38] E.P. Barrett, L.G. Joyner, P.P. Halenda, J. Am. Chem. Soc. **73** (1951) 373.
[39] K.V.S. Sastry, D.W. Fuerstenau, "Pelletization of fine coals", Report EPRI CS-2198 Res. Proj. 1030, Un. California, Berkeley (1982)
[40] P. Müller, S. Antonyuk, J. Tomas, Chem. Eng. Technol. **34** (2011) 1543
[41] L.H. Smith, *Inorganic syntheses*, John Wiley Sons, New York (1983).
[42] Y. Jin, L. Li, Z. Liu, S. Zhu, D. Wang, Adv. Powder Technol. **32** (2021) 791.
[43] S.M. Al-Jubouri, H.A. Sabbar, H.A. Lafta, B.I. Waisi, Desalin. Water Treat. **165** (2019) 290.
[44] I. Majchrzak-Kucęba, W.J. Nowak, Therm. Anal. Calorim. **77** (2004) 125.
[45] C. Kosanović, B. Subotić, A. Čižmek, Thermochim. Acta **276** (1996) 91.
[46] D.W. Breck, *Zeolite molecular sieves*, Wiley, New York (1974).
[47] Z. Jiang, J. Yang, H. Ma, X. Ma, J. Yuan, Clean Techn. Environ. Policy **18** (2016) 629.
[48] G.X. Zhang, D. Tang, G. Jiang, Adv. Powder Technol. **24** (2013) 689.
[49] Q. Tian, K. Sasaki, Environ. Sci. Pollut. Res. **26** (2019) 23542.
[50] T. Hu, W. Gao, X. Liu, Y. Zhang, C. Meng, R. Soc. Open Sci. **4** (2017) 1.
[51] B. Jha, D.N. Singh, J. Mater. Educ. **33** (2011) 65.
[52] M. Thommes, K. Kaneko, A.V. Neimark, J.P. Olivier, F. Rodriguez-Reinoso, J. Rouquerol, K.S. Sing, Pure Appl. Chem. **87** (2015) 1051.
[53] M.V.B. Gonçalves, A.V. Cardoso, F.V. Parreira, Cerâmica **66**, 378 (2020) 93.
[54] P. Müller, A. Russell, J. Tomas, Chem. Eng. Sci. **126** (2015) 204.
[55] A. Russell, J. Schmelzer, P. Müller, M. Krüger, J. Tomas, Powder Technol. **286** (2015) 546.
[56] S. Antonyuk, J. Tomas, S. Heinrich, L. Mörl, Chem. Eng. Sci. **60** (2005) 4031.
[57] F. Akhtar, L. Andersson, S. Ogunwumi, N. Hedin, J. Eur. Ceram. Soc. **34** (2014) 1643.
[58] N.L. Michels, S. Mitchell, M. Milina, K. Kunze, F. Krumeich, F. Marone, M. Erdmann, N. Marti, J. Perez-Ramirez, Adv. Funct. Mater. **22** (2012) 2509.
(Rec. 21/02/2022, Rev. 18/05/2022, 27/06/2022, Ac. 29/06/2022)